Chemical Geology 283 (2011) 161–170

Contents lists available at ScienceDirect

Chemical Geology

journal homepage: www.elsevier.com/locate/chemgeo

Research papers

Polymerization of aqueous silica in H_2O–K_2O solutions at 25–200 °C and 1 bar to 20 kbar

Jonathan D. Hunt [a,*], Abby Kavner [a,b], Edwin A. Schauble [a], Don Snyder [c], Craig E. Manning [a]

[a] Department of Earth and Space Sciences, University of California, Los Angeles, CA 90095-1567, United States
[b] Institute of Geophysics and Planetary Physics, University of California, Los Angeles, CA 90095, United States
[c] Rand Corp, 1776 Main Street, Santa Monica, CA 90401, United States

ARTICLE INFO

Article history:
Received 17 September 2010
Received in revised form 22 December 2010
Accepted 29 December 2010
Available online 7 January 2011

Editor: J. Fein

Keywords:
Raman spectroscopy
Aqueous silica polymerization
Diamond anvil cell
Alkaline fluids
Ab initio calculation

ABSTRACT

Understanding the polymerization of aqueous silica is important for modeling fluid–rock interactions at high pressure and temperature. However, it remains unclear how changes in SiO_2 concentration, alkalinity, pressure, and temperature affect silica polymerization and depolymerization. We studied silica speciation in alkaline K_2O–SiO_2–H_2O solutions at ambient conditions (0.05, 0.5 and 5 molal Si, 0.5–0.8 K_2O/SiO_2), as well as at elevated pressure and temperature in a diamond anvil cell (5 molal Si, $K_2O/SiO_2 = 0.7$). The controls on polymerization were assessed by comparing Raman spectroscopic results to ab initio calculations that focused on four neutral species: the monomer, the dimer, and the linear and ring trimers. In addition to a ~785 cm^{-1} band associated with Si–OH symmetric stretching in the monomer, the calculations show that Si–O–Si stretching in the dimer and trimers yields peaks at ~600 cm^{-1}. A broad 600 cm^{-1} feature has been observed in previous studies at high pressure and temperature, and the broadness has been attributed to a soft Si–O–Si angle in the dimer and temperature; however, our calculations show that this is not alone sufficient to explain this feature, and that other species likely contribute. The breathing mode of the ring trimer yields an additional feature at ~500 cm^{-1}, which may be representative of contributions from highly polymerized species to the low-frequency limb of the broad 600 cm^{-1} feature. Individual Si–OH stretching and bending in all species gave features at ~825–875 cm^{-1} and ~950–1050 cm^{-1}. These bands overlap significantly with $Si–O^-$ stretching modes of deprotonated species, which are more abundant in the alkaline solutions studied experimentally. Measured Raman spectra at ambient conditions display broad peaks associated with monomers (735–800 cm^{-1}), oligomers (475–650 cm^{-1}) and deprotonated species (850–1125 cm^{-1}). Peak areas attributed to oligomers and deprotonated species increase linearly with total Si concentration, with a small dependence on the K_2O/SiO_2 ratio, indicating that Raman intensities are proportional to species concentrations. The Raman peak area of the monomer feature does not scale linearly with total SiO_2 concentration, however, and depends strongly on the K_2O/SiO_2 ratio. In broad agreement with NMR results, the Raman spectra show that increasing silica concentration promotes silica polymerization, and that increasing the K_2O/SiO_2 ratio or temperature depolymerizes aqueous silica. The Raman spectra show that increasing pressure also causes aqueous silica to depolymerize. The results provide a foundation for characterizing aqueous silica polymerization at crustal and upper mantle conditions.

1. Introduction

Water-rich fluids have the capacity to dissolve significant amounts of rock-forming minerals at the pressures (P) and temperatures (T) of the Earth's lower crust and upper mantle. A major constituent of these fluids is silica, even in quartz-undersaturated systems (Anderson and Burnham, 1965; Manning, 1994; Newton and Manning, 2002). Silica in concentrated, high P–T aqueous solutions is extensively polymerized (Zhang and Frantz, 2000; Zotov and Keppler, 2000, 2002; Newton and Manning, 2002, 2003, 2008), which has important effects on metamorphism and metasomatism in the crust and mantle. Polymerization not only enhances the potential for silica mass transfer (Newton and Manning, 2002, 2003), but it also promotes the mobility of other rock-forming oxides, including those that are nominally insoluble (e.g. Al_2O_3 and TiO_2) (Manning, 2004, 2007; Manning et al., 2008, 2010).

At equilibrium at the P and T of crustal metamorphism, neutral-pH fluids in the system SiO_2–H_2O are inferred to contain chiefly monomers, $Si(OH)_4$, and dimers, $Si_2O(OH)_6$ (Fig. 1a,b; Zotov and Keppler, 2000, 2002; Newton and Manning, 2002, 2003; Tossell, 2005). However, more polymerized species have been proposed (e.g., Gerya et al., 2005), and within ~100 °C of the hydrothermal melting of quartz (Kennedy et al., 1962), ring trimers are hypothesized to predominate (Newton and

* Corresponding author. Tel.: +1 310 487 3864; fax: +1 310 825 2779.
E-mail address: jhunt@ess.ucla.edu (J.D. Hunt).

0009-2541/$ – see front matter © 2011 Elsevier B.V. All rights reserved.
doi:10.1016/j.chemgeo.2010.12.022

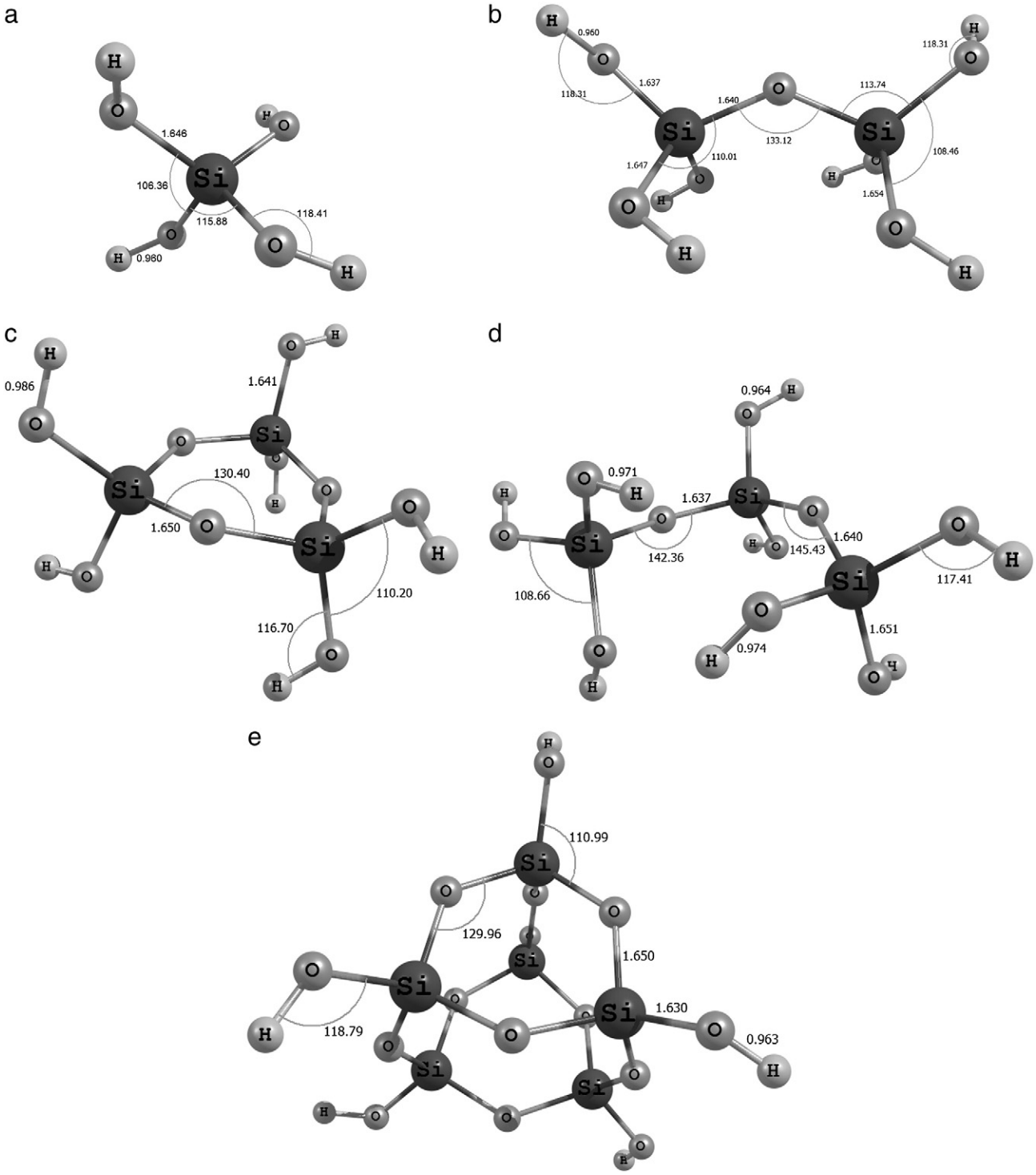

Fig. 1. Structures of a.) the $Si(OH)_4$ monomer, b.) the $Si_2O(OH)_6$ dimer, c.) the $Si_3O_3(OH)_6$ ring trimer, d.) the $Si_3O_2(OH)_8$ "linear" chain trimer, and e.) the $Si_6O_6(OH)_6$ cage hexamer, optimized using B3LYP density functional theory in the gas phase.

Manning, 2008). Species containing three and four Si-tetrahedra are inferred in more complex, multicomponent solutions (e.g., Mysen, 1998; Mibe et al., 2008), and it has been suggested that proximity to the melting point in the system Na_2O–Al_2O_3–SiO_2–H_2O may be linked to the abundance and extent of oligomerization (Manning et al., 2010). However, such studies are largely reconnaissance in nature — partly because of experimental challenges of working at the required high *P* and *T*, but also because of an absence of studies linking oligomerization at high *P* and *T* to established observations of oligomerization in highly alkaline fluids at ambient conditions. Although highly alkaline, Si-rich fluids are geologically uncommon, they can provide insight into silicate polymerization in other contexts where Si concentrations may be high, such as crustal and mantle fluids.

It has long been known that dissolved silica polymerizes in Si-rich alkaline solutions at ambient and low- *T* (e.g., Iler, 1979). In addition to the monomer and dimer (e.g., Alexander, 1954; Alexander et al., 1954; De Almeida and O'Malley, 1993; Tossell and Sahai, 2000; Sefcik and Goddard, 2001), ring ($Si_nO_n(OH)_{2n}$), chain ($Si_nO_{n-1}(OH)_{2n+2}$), and cage ($Si_{2n}O_{3n}(OH)_{2n}$) oligomers (Fig. 1c–e) appear at high concentrations (Ray and Plaisted, 1983; Dutta and Shieh, 1985; Kinrade and

Swaddle, 1988a; Kinrade and Pole, 1992; Tanaka and Takahashi, 1999; Provis et al., 2005; Cho et al., 2006; Haouas and Taulelle, 2006; Knight et al., 2007). Much of our understanding of the speciation, kinetics, and mechanisms of silicate polymerization at these conditions comes from nuclear magnetic resonance (NMR) spectra (e.g. Harris and Knight, 1983a,b; Kinrade and Swaddle, 1988a,b; Kinrade and Pole, 1992; Vallazza et al., 1998; Cho et al., 2006; Haouas and Taulelle, 2006), which has led to the identification of forty-eight geometrically distinct silicate oligomers (Knight et al., 2007). This body of work shows that, in general, polymerization is favored by high SiO_2 concentrations, low alkalinity, and low temperatures (Kinrade and Swaddle 1988a).

Unfortunately, NMR studies have not been extended to geologically relevant high *P*–*T* conditions. In part, this is because, above ~150 °C, it becomes difficult to obtain ^{29}Si-NMR spectra due to rapid silicon exchange on the NMR timescale, resulting in the loss of structural information (Kinrade and Swaddle, 1988b; Vallazza et al., 1998). High *P* and *T* are readily attained in the hydrothermal diamond anvil cell (Bassett et al., 1993), however, and the transparency of diamond allows fluids and solutes to be studied *in situ* by optical and other spectroscopic methods. Raman spectroscopy has proven especially useful in the study of aqueous silica (e.g., Zotov and Keppler, 2000, 2002; Mysen 2010); however, interpretation of spectra is hindered by uncertainties in the systematic compositional controls on species identities and extent of polymerization. Especially important is the lack of systematic Raman spectroscopic studies of silica polymerization at high pH and high SiO_2 concentrations, similar to those investigated by NMR studies at ambient conditions to moderate *T*.

In this study, we collected Raman spectra at ambient conditions on a series of potassium-silicate solutions with varying silicate concentrations (0.005–5.0 molal Si) and K_2O/SiO_2 molar ratios of 0.5, 0.6, 0.7, and 0.8. We used density functional theory computational techniques to calculate Raman spectra for various neutral silicate species to predict how polymerization alters the Raman spectra of aqueous silica, and to compare directly with the measured Raman spectra. We also collected Raman spectra of a single solution ($[SiO_2] = 5$ molal, $K_2O/SiO_2 = 0.7$) in a diamond anvil cell at elevated *P* (2–20 kbar), and elevated *T* (to 200 °C). Together, the measurements and the calculations offer insights into the mechanisms of silica polymerization relevant to crustal and mantle fluids.

2. Methods

2.1. Solution preparation

LUDOX TM50 colloidal silica sol was dissolved with KOH (Sigma-Aldrich) in distilled, deionized H_2O to produce solutions with a range of K_2O/SiO_2 ratios, total Si concentration, and pH (Table 1). The sol is composed of solid, amorphous silica spheres (50% by weight, sphere radius ~10 nm) suspended in aqueous solution, which are stabilized by trace Na_2O. Prior to mixing, the undissolved, suspended silica sol particles show no resolvable Raman features in the spectral region of interest (400–1200 cm^{-1}). Upon addition of KOH to the sol, the spheres rapidly flocculated, producing a high pH (11–14) supernatant solution. With five to ten minutes of vigorous stirring, the precipitated silica completely dissolved in the supernatant liquid and remained in solution until analysis. Stored in polyethylene bottles, the solution remains stable indefinitely, without any detectable change in the Raman signal. This method allows us to sample a wide range of Si concentrations and pH. The solution pH was determined with a handheld pH meter at ambient conditions, calibrated to pH 7 and 10. No correction was made for alkali-metal error. Though the alkali-metal error is lower for potassium than for smaller alkali metals, the uncertainty in measured pH values may be as much as half of a pH unit (Licht, 1985), especially at the highest SiO_2 concentrations and K_2O/SiO_2 ratios.

Table 1
Measured pH of silicate solutions.

$[SiO_2]$ (molal)	K_2O/SiO_2 ratio			
	0.5	0.6	0.7	0.8
5	13.3	13.8	14.0	14.1
4	13.2	13.7	13.9	14.0
3	13.0	13.6	13.7	13.9
2	12.8	13.4	13.5	13.7
1	12.6	13.1	13.3	13.4
0.5	12.4	12.8	13.1	13.2
0.1	11.8	12.2	12.5	12.6
0.05				12.3
0.01				11.7
0.005				11.4

2.2. Raman spectroscopy

Raman spectroscopy was carried out using a microscope-based confocal Raman spectroscopy system at UCLA. The excitation source is the 488 nm line of a 5 W Spectra Physics Ar^+ laser, operating at an output of 400 mW. The filtered beam is directed into the body of an Olympus BM microscope, and directed through a Mitutoyo 20× objective lens and onto the sample with a spot size ~2 μm. Backscattered Raman signal (180° geometry) is then collected by the objective and directed through a confocal imaging system equipped with a ~200 μm pinhole. We estimate the power at the sample to be ~50 mW. The Raman signal is collected in a 50 μm wide entrance slit into an Acton 2750 spectrometer, dispersed via the 1200 grooves/mm grating, and collected using a Peltier-cooled CCD Princeton Instruments (PIXIS) detector. With this geometry, the spectral width is approximately 1200 cm^{-1} and the resolution is ~2 cm^{-1}. Wavelength calibration of the spectrometer was performed before each set of experiments using a neon lamp.

To acquire the spectra at ambient conditions, the silica solutions were transferred into glass cuvettes with a sample volume of 3.5 ml and placed at the objective focal spot. The exposure time for concentrated solutions ($[SiO_2] \geq 0.1$ molal) was 60 accumulations of 5 s each. For dilute solutions, the exposure time was increased to 60 accumulations of 15 s each. Pure water backgrounds were acquired before and after each solution spectrum, and the average water spectrum was subtracted before performing a smoothed spline background subtraction. The identical collection times, laser power, and background subtractions allow peak heights and areas to be compared between silicate spectra, though due to the tripled collection time, the peak areas of the dilute solutions could not be compared directly with the peak areas of the concentrated solutions. Peak areas are measured as the integral of the background-corrected spectrum over the frequency range of interest; no attempt was made to fit the peaks to Gaussian or Lorentzian functions.

For spectral acquisition at elevated *P*, or *P* and *T*, the silica solutions were loaded into externally heated diamond anvil cells (Bassett et al., 1993) using steel gaskets with 500 μm initial thickness and a 250 μm diameter hole to contain the sample. Pressure was measured at ambient *T* by the ruby fluorescence method to within ±1.5 kbar (Mao et al., 1978). At elevated *T*, pressure was calculated by assuming that the sample chamber is isochoric (Bassett et al., 1993) and that fluid properties can be approximated by a pure-water equation of state (Gerya et al., 2005). No detectable dissolution of ruby was observed. Temperature was measured with K-type thermocouples attached to each diamond. Exposure time in all diamond cell experiments was 60 accumulations of 5 s each.

2.3. Ab initio calculations

Raman spectra of neutral silicate species were calculated ab initio to assist interpretation of the experimental data. All calculations were

performed with Gaussian 03 (Frisch et al., 2004) using hybrid B3LYP density functional theory (Becke, 1993). Solvation effects were incorporated in two separate ways for each species. The first was through an integral-equation-formalism polarizable-continuum model (IEF-PCM) (Cances et al., 1997; Mennucci et al., 1997; Mennucci and Tomasi, 1997; Tomasi et al., 1999), used to simulate implicitly the bulk properties (e.g., the dielectric constant) of the solvent. All implicit-solvation calculations were done with properties of water at 25 °C; trial calculations using the dielectric constant of water at 950 °C did not meaningfully change the geometry or vibrational frequencies. Solvation effects were also simulated by adding four water molecules to gas-phase simulations. This explicitly incorporated solution properties arising from the presence of an inner hydration shell. Trial calculations with eight water molecules revealed little difference from spectra calculated using four water molecules; incorporation of four water molecules was therefore judged sufficient for the purposes of this study, though it should be noted that a full inner hydration shell would contain many more than eight water molecules, especially for non-monomeric silicate species. Ideally, solution effects would be incorporated by simultaneous use of a polarizable-continuum model with an inner hydration shell of explicit water molecules, but this approach was precluded by the much greater computational overhead. All calculations were done with either the 6–311++G(d,p) or 6–31++G(d,p) basis sets; the smaller set was chosen when the larger set would be computationally prohibitive (Krishnan et al., 1980). Comparison tests showed that choice of basis set yielded no significant difference in calculated Raman frequencies or intensities. Our calculations focused on neutral species. Neutral species are subordinate components of the experimentally studied, alkaline solutions; however, models of charged species in the gas phase suggest that, in addition to producing distinct, high-frequency peaks due to Si–O^- vibrations, deprotonated species also have Raman-active modes for core Si–O* structural vibrations that are similar to those of neutral species. Deprotonated species were therefore not considered further in our ab initio calculations.

Although ab initio methods typically overestimate experimental vibrational frequencies by ~5 to 10% for small gas-phase molecules (Scott and Radom, 1996), we found in contrast that the B3LYP calculations underestimated the experimental vibrational frequency of the symmetric stretching modes of the $Si(OH)_4$ and $Al(OH)_4^-$ monomers by 4.5%. We applied this value as a constant scaling factor to all calculated Raman frequencies of all aqueous silicate species. Adding implicit solvation via a polarizable continuum model does not appear to change the accuracy of calculated frequencies, but it does improve the accuracy of energy calculations (Tossell and Sahai, 2000; Tossell, 2005). In general, the implicitly solvated spectra appear to have higher Raman activities than either the gas phase or explicitly solvated spectra. This could possibly be due to the dielectric field applied around the molecule, enhancing its polarizability. To construct Raman spectra from the frequency data, the peaks were assumed to have a Lorentzian shape, and an arbitrary full width at half height of 30 cm^{-1} was chosen.

3. Results

3.1. Ab initio calculations

3.1.1. Monomer

The three Raman spectra calculated for the $Si(OH)_4$ monomer – in the gas phase, with the polarizable continuum model, and with explicit solvation – all display a single prominent feature corresponding to symmetric stretching of the Si–OH bonds at 756, 753, and 742 cm^{-1}, respectively, which were then averaged and scaled by 4.5% to match the accepted experimental value of ~785 cm^{-1}. This agrees with previous experimental and calculated results (e.g. Dutta and Shieh, 1985; Zotov and Keppler, 2000, 2002; Tossell, 2005). In the gas phase, the $Si(OH)_3O^-$ and the $Si(OH)_2O_2^-$ monomers each have a symmetric Si–O* stretch feature with a similar intensity to the symmetric stretch of the neutral monomer, shifted down to 694 and 611 cm^{-1}, respectively. New strong features, due to Si–O^- stretching, arise at 1141 cm^{-1} in the singly deprotonated monomer and at 928, 935, and 1086 cm^{-1} in the doubly deprotonated monomer.

3.1.2. Dimer

Experimental Raman spectra of polymerized silica in solution yield a peak at ~600 cm^{-1} over a wide range of *P* and *T* (Dutta and Shieh, 1985; Zotov and Keppler, 2000, 2002). Fig. 2 shows calculated spectra of the dimer in the gas phase and in H_2O, solvated using either IEF-PCM or explicit water molecules. All display a prominent feature corresponding to the Si–O–Si stretch between ~590 and ~680 cm^{-1}. Regardless of the solvation model, the calculated frequency of the Si–O–Si stretch feature is lower for the solvated dimer, in which the minimum-energy Si–O–Si angle is ~165°, than for the dimer in the gas phase, in which the Si–O–Si angle is ~130°. A gas phase calculation in which the Si–O–Si angle was fixed at 165° yielded a frequency of 604 cm^{-1} (Fig. 2), suggesting that the calculated shift chiefly depends on Si–O–Si bond angle rather than solvation.

To test this, we calculated the variation in frequency with Si–O–Si bond angle for the gas phase and implicitly and explicitly solvated dimers. Once the optimal dimer structure was found, the bridging angle was systematically varied, and the rest of the molecule was optimized while keeping the bridging angle fixed at the perturbed value. This yielded the lowest energy structure possible for each bridging angle. Raman spectra were then calculated for each resulting structure. As shown in Fig. 3, the frequency of the Si–O–Si symmetric stretch decreases with increasing Si–O–Si bond angle in all three cases. Previous experimental observations of a feature at ~600 cm^{-1} (Dutta and Shieh, 1985; Zotov and Keppler 2000, 2002) thus imply a high Si–O–Si angle in the dimer in solution over a range of *P* and *T*. Our results are consistent with the observed shift in peak frequency with reduction in Si–O–Si bond angle in solid silicates (Lazarev, 1972; Furukawa et al., 1981, Zotov et al., 1996).

All calculated dimer spectra also show features from ~850 cm^{-1} to ~1000–1050 cm^{-1}, corresponding to Si–OH stretching and bending. The frequencies of these features seem to depend on both the Si–O–Si angle and the method of solvation, probably because these modes will depend on the specific local solvation environment around the Si–OH

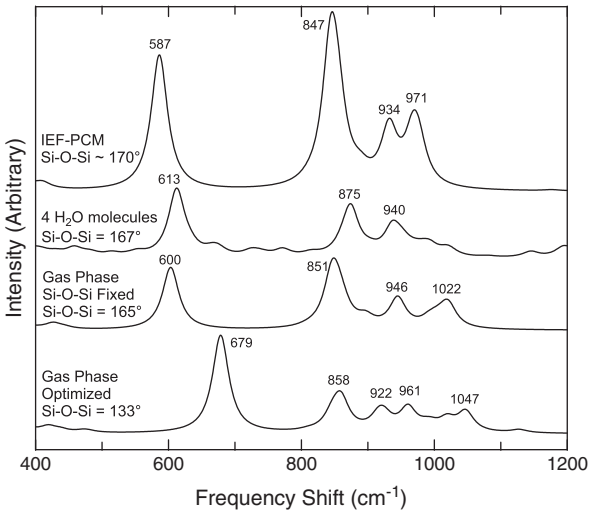

Fig. 2. Calculated Raman spectra for the dimer, $Si_2O(OH)_6$, in the gas phase (with two different Si–O–Si bridging angles) and solvated using either a polarizable continuum model or explicit water molecules. All simulations were optimized using B3LYP density functional theory. The 6–311++G(d,p) basis set was used for the gas phase and PCM calculations, and the smaller 6–31++G(d,p) basis set was used for the explicit solvation calculation.

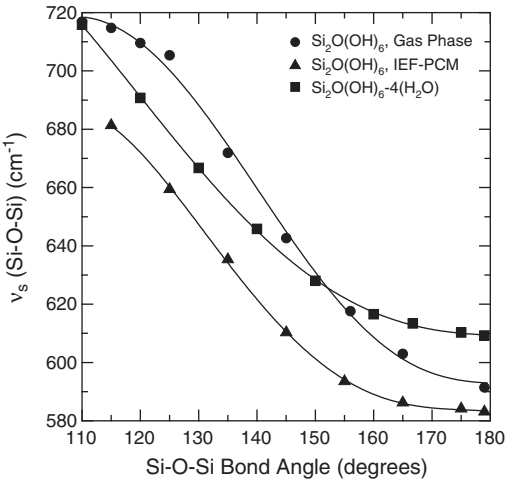

Fig. 3. Calculated frequencies of the Si–O–Si symmetric stretch in the $Si_2O(OH)_6$ dimer as a function of Si–O–Si angle for the gas phase, PCM, and explicitly solvated species. The 6–311++G(d,p) basis set was used for the gas phase and PCM calculations, and the smaller 6–31++G(d,p) basis set was used for the explicit solvation calculation.

bond. This may tend to dampen the signal from these modes in an experimental solution.

3.1.3. Trimer and tetramer

Fig. 4 shows calculated gas-phase spectra for the ring and linear trimers as well as two geometries of ring tetramer, one with all Si atoms in a single plane, and the other with the Si atoms in a 'puckered' arrangement, between planar and tetrahedral geometries. Both of these structures are optimized, but the 'puckered' tetramer has a higher energy. Both the linear and ring trimers display a prominent feature at ~600 cm^{-1}, due to the Si–O–Si symmetric stretch. This signal coincides with the main dimer peak at ~600 cm^{-1}, and poses difficulties for deconvolving contributions to an observed ~600 cm^{-1} peak from individual oligomeric species. The ring trimer displays an additional feature at ~500 cm^{-1}, due to the asymmetric ring breathing mode. The frequency of the ring breathing mode in the ring tetramer depends on the local geometry. It is therefore likely that ring breathing modes will, in general, be located in the 500–600 cm^{-1} range, and that deconvolving the modes from individual species will be difficult, due to high variability in local geometry. All calculated trimer and tetramer spectra also show features from ~800–850 cm^{-1} to ~1050 cm^{-1}, corresponding to Si–OH stretching and bending. These are not significantly different from analogous features in the calculated dimer spectra, given the variability of the peak locations in the dimer spectra. It therefore appears that it would be difficult to deconvolve peaks in the 800–1050 cm^{-1} range into contributions from differently polymerized species (e.g. Q^1 and Q^2, where Q^n refers to a single silica tetrahedron bound to *n* other tetrahedra via bridging oxygens) based on our calculated spectra.

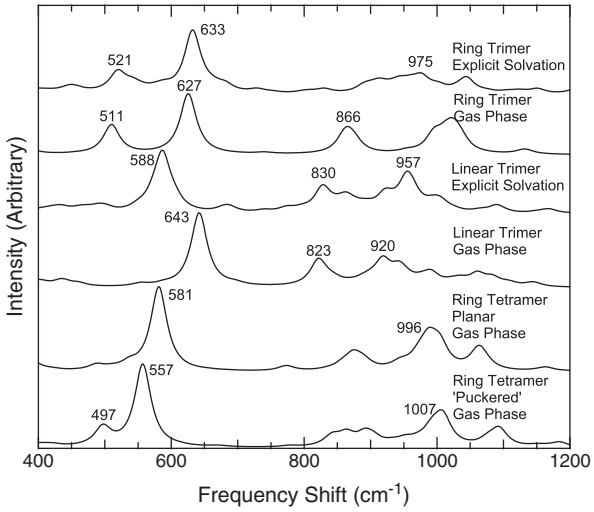

Fig. 4. Calculated Raman spectrum for the ring and linear trimers, $Si_3O_3(OH)_6$ and $Si_3O_2(OH)_8$, respectively, optimized using B3LYP density functional theory with the 6–31++G(d,p) basis set in the gas phase, and using explicit solvation. Calculated spectra are also shown for two geometries of the ring tetramer, $Si_4O_4(OH)_8$, both optimized using B3LYP density functional theory with the 6–31++G(d,p) basis set in the gas phase.

3.2. Experimental Raman spectroscopy

Raman spectra were collected from a series of solutions with varying total Si concentrations (0.05, 0.5, and 5 molal) and K_2O/SiO_2 ratios at ambient conditions (Fig. 5). The variations in solution composition yielded systematic changes in three spectral regions, corresponding to –Si–O–Si– vibrational modes in oligomers (475–650 cm^{-1}), Si–O* symmetric stretching in the monomer (750–800 cm^{-1}), and Si–O^- stretching in all deprotonated species (850–1125 cm^{-1}) (Fig. 5). The Raman spectrum of the most dilute solution ([Si] = 0.05 molal; Fig. 5a) shows a prominent feature at ~785 cm^{-1}, corresponding to the

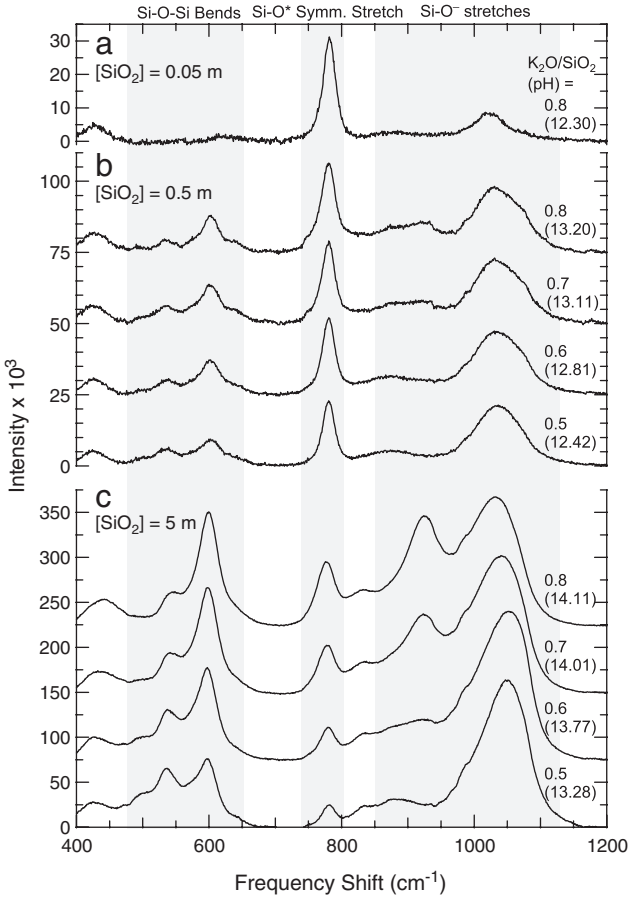

Fig. 5. Raman spectra of high-pH silicate solutions taken at ambient conditions. The concentration of SiO_2 in each figure remains constant, though the spectra are scaled for clarity. a.) shows [SiO_2] = 0.05 molal at a K_2O/SiO_2 ratio of 0.8, b.) shows [SiO_2] = 0.5 molal with K_2O/SiO_2 from 0.5 to 0.8, and c.) shows [SiO_2] = 5 molal with K_2O/SiO_2 from 0.5 to 0.8. The spectra in b.) and c.) were created using 60 accumulations of 5 s each, while the spectrum in a.) was created using 60 accumulations of 15 s each. The spectral features of note are the monomer symmetric stretch at ~785 cm^{-1}, the oligomer symmetric stretch at ~600 cm^{-1}, and the possible ring breathing modes at 500–550 cm^{-1}. The large peaks at ~925 cm^{-1} and ~1100 cm^{-1} are due to the Si–O^- stretches in deprotonated species ($Si(OH)_3O^-$, $Si_2O(OH)_5O^-$, $Si(OH)_2O_2^{2-}$, etc.), a consequence of the high pH.

monomer symmetric stretch (Dutta and Shieh, 1985; De Almeida and O'Malley, 1993; Zotov and Keppler, 2000, 2002). The spectrum also shows a weak feature at ~600 cm^{-1}, consistent with the dimer/oligomer symmetric stretch (Dutta and Shieh, 1985; Zotov and Keppler, 2000, 2002; Figs. 2 and 4). Spectra at higher concentrations (Fig. 5b and c) show the same features but with varying intensity, as well as additional low-frequency oligomeric features at 500–550 cm^{-1}, probably due to ring breathing modes (Dutta and Shieh, 1985; Fig. 4). According to Dutta and Shieh (1985), the large peak observed at 1000–1100 cm^{-1} is due to Si–O^- stretches in deprotonated oligomer species (e.g., $Si_2O(OH)_5O^-$, $Si_3O_3(OH)_4O_2^{2-}$). They assign the ~925 cm^{-1} peak to symmetric stretching of the two Si–O^- bonds in the doubly deprotonated monomer ($Si(OH)_2O_2^{2-}$). In the present study, the ~925 cm^{-1} peak is only clearly resolved in solutions with measured pH above ~13.5. This is similar to the second pK_a of the monomer as determined by Sjoberg et al. (1983), consistent with the interpretation of Dutta and Shieh.

Comparison of Fig. 5b and c (Fig. 5a is not directly comparable due to its acquisition with a tripled collection time) shows that with a tenfold increase in total Si concentration, the ratio of the oligomer peak height to the monomer peak height increases from roughly fourfold (at $K_2O/SiO_2 = 0.8$), to nearly eightfold (at $K_2O/SiO_2 = 0.5$). This highlights the expected dependence of silica polymerization on the total concentration of silica in solution as well as the K_2O/SiO_2 ratio. As alkalinity increases at the same total [Si], the silica depolymerizes, as evidenced by the increase in monomer peak height in concert with the decrease in ring oligomer peak height.

A 5 molal Si solution with $K_2O/SiO_2 = 0.7$ was studied in the hydrothermal diamond anvil cell at elevated *P* and *T* (Fig. 6a), and elevated *P* at ambient *T* (Fig. 6b). Difference spectra show that the monomer peak area increases with rising *P* at constant *T*, and with rising *T* and nearly constant *P*. In addition, the monomer peak position shifts to slightly higher frequency with *P* at 25 °C ($\Delta\nu$ ~ 1.5 cm^{-1}/kbar), but to lower frequency as *T* increases at 8.4–10 kbar ($\Delta\nu$ ~ −0.06 cm^{-1}/°C). These trends are qualitatively similar to shifts of the 464 cm^{-1} Raman line of quartz with *P* ($\Delta\nu$ ~ 0.9 cm^{-1}/kbar) and *T* ($\Delta\nu$ ~ −0.0154 cm^{-1}/°C) (Schmidt and Ziemann, 2000), though the absolute frequency shifts are higher. This may be because aqueous silica solutions are more compressible than solid quartz.

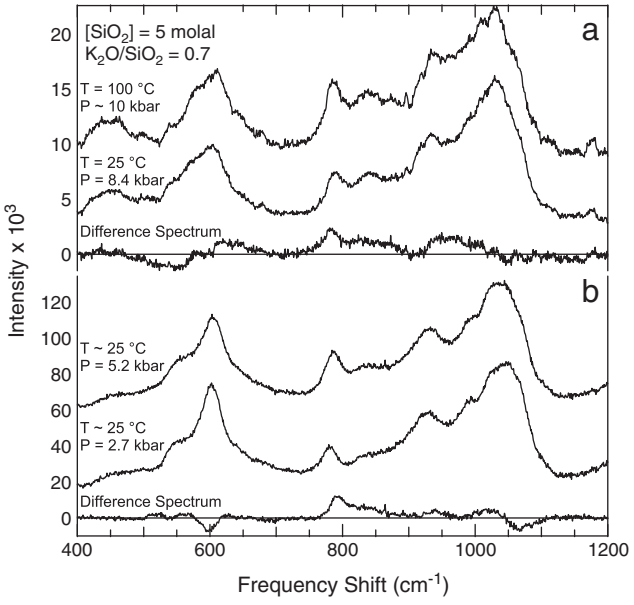

Fig. 6. Raman spectra of a silicate solution ($[SiO_2] = 5$ molal, $K_2O/SiO_2 = 0.7$) in a diamond anvil cell at a.) elevated *P* and *T*, and b.) elevated *P* and ambient *T*. The spectra were created using 60 accumulations of 5 s each. The difference spectrum in a.) shows an increase in the monomer peak height, an increase in the average oligomer peak frequency, and a decrease of the monomer peak frequency with increasing *T*. The difference spectrum in b.) shows an increase in the monomer peak height, a decrease in the oligomer peak height, and an increase of the monomer peak frequency with increasing *P* at room *T*.

4. Discussion

4.1. Comparison of computational and experimental spectra

4.1.1. Deprotonated monomers

Calculations in the gas phase show that the frequency of the symmetric stretch of Si–O* bonds in the monomer shifts significantly downward as the monomer becomes more negatively charged (~60 to 150 cm^{-1} shift). In the pH range of the experimental solutions (11.3 to 14.1), singly and doubly deprotonated monomers should be far more abundant than neutral monomers. However, there are no peaks in any experimental spectrum between 650 and 750 cm^{-1}, and no pH-dependent shift of the experimental ~785 cm^{-1} peak was observed (Fig. 5a). Moreover, the experimental peak at ~785 cm^{-1} is at its greatest intensity at pH 14.1. It therefore appears likely that the Si–O* symmetric stretch of the deprotonated monomers are contributing to the experimental peak at ~785 cm^{-1}. Using gas phase models to describe deprotonated species in concentrated aqueous solutions likely introduces significant error.

4.1.2. Si–O^- and Si–OH stretching

Fig. 7 shows an example comparison of our experimental and calculated spectra of neutral species. The relative weight of each individual calculated spectrum was chosen to match approximately the experimentally observed intensity ratio of monomer and oligomer bands at ~785 and ~600 cm^{-1}, respectively. Additional Q^2 and Q^3 species are known to be present at these conditions (Kinrade and Swaddle, 1988a; Knight et al., 2007), so the comparison is only approximate. Nevertheless, the comparison reveals that the greatest discrepancy between the calculated spectra for neutral species and the observed spectrum is the absence of calculated high-intensity features at ~950–1100 cm^{-1}, consistent with the assignment of this feature to deprotonated species (Dutta and Shieh, 1985), which were not included in the calculations. Our calculations suggest that Si–OH stretching in neutral species produces peaks in the 800–1050 cm^{-1}

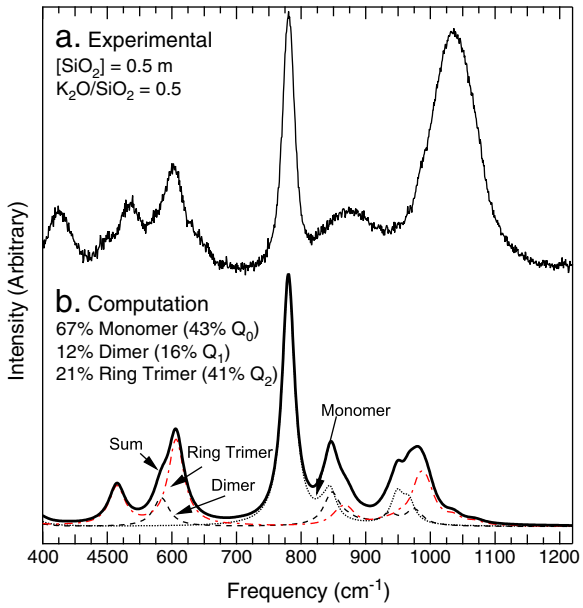

Fig. 7. Visual comparison between a.) a single experimental spectrum ($[Si] = 0.5$ molal, $K_2O/SiO_2 = 0.5$), and b.) a sum of calculated spectra in the following proportions: 67% monomer (43% Q^0), 12% dimer (16% Q^1), and 21% ring trimer (41% Q^2). The percentages of Q^n species shown are recalculated based on the number of Si tetrahedra in the monomer, dimer, and ring trimer.

range, in general agreement with the assignments of Mysen (2010); however, it is not possible to assign any individual peak to a single species or Q^n, due to band overlaps. We have not considered the Si–OH stretching of Q^3 (cage) species in our calculated spectra, and there may also be a signal from Si–OH stretching of Q^3 species around 1050 cm^{-1}, as Mysen suggests. However, because there is likely a suite of species with deprotonation signals, due to the high pH, as well as a suite of cage species (Knight et al., 2007), it may be impossible to deconvolve the large experimental peak at 1050 cm^{-1} into two or more distinct signals and conclusively assign them to specific species.

4.1.3. Oligomer peak shape

The spectra with $K_2O/SiO_2 = 0.5$ in Fig. 5 clearly show the ~600 cm^{-1} Si–O–Si symmetric stretch, as well as a separate peak at ~525 cm^{-1}. Following Dutta and Shieh (1985), and supported by our ring trimer and tetramer calculations (Fig. 4) as well as studies of ring structures in solid amorphous silica (Galeener et al., 1984), we assigned the latter to general ring oligomer breathing modes, although separate breathing modes may also contribute to the peak at 600 cm^{-1} (Fig. 4). As the K_2O/SiO_2 ratio increases, the ~525 cm^{-1} peak is reduced in intensity and shifts slightly upward in frequency, creating a shoulder on the ~600 cm^{-1} peak.

In the H_2O–SiO_2 system at high *P* and *T*, Zotov and Keppler (2000, 2002) observe a single very broad peak centered around 600 cm^{-1}. They assigned the peak to the dimer and attributed its broadness to a shallow potential energy surface along the dimer bridging-angle coordinate, noting that the frequency of the Si–O–Si vibration decreases with increasing Si–O–Si bond angle; however, they could not rule out contributions from higher-order oligomers. The presence of separate peaks at 525 and 600 cm^{-1} at low K_2O/SiO_2 (Fig. 5) suggests that distinct contributions from several sources must be considered.

To determine whether a soft Si–O–Si angle could account for the broad peak at ~600 cm^{-1} observed by Zotov and Keppler, we calculated Raman spectra that take the potential energy surface into account. Following the method used to derive Fig. 3, a potential energy surface along the one degree of freedom given by the bridging angle variation was constructed (Fig. 8). A Boltzmann distribution was used to determine the relative population of bridging angles, and calculated Raman frequencies (Fig. 3) were interpolated and combined over all bridging angles to provide a peak width at any given temperature. Since the Boltzmann distribution is dependent on temperature, the peak will broaden as temperature is raised. At 1000 °C, the gas phase model dimer will have a significant population between ~120° and 180° (Fig. 8), which will result in a peak that spans ~100 cm^{-1} (Fig. 3). The IEF-PCM and explicitly solvated model dimers have significant populations between ~140° and 180° at 1000 °C (Fig. 8). The peaks for these models, however, only span ~30 cm^{-1} due to the smaller shift in frequency at large Si–O–Si angles (Fig. 3). Furthermore, even the gas phase spectrum shows significant broadening only *above* ~600 cm^{-1}, whereas Zotov and Keppler observed broad peaks from 500 cm^{-1} to 700 cm^{-1}. Our ab initio results therefore suggest that additional ($Si_{n>2}$) species contribute to the shoulder at lower wavenumbers, while the shallow potential energy surface of the bridging angle could only be responsible for broadening at higher wavenumbers. This is consistent with evidence from NMR studies for ($Si_{n>2}$) species in ~1 molal potassium silicate solutions at ambient pressure and temperature (Knight et al., 2007).

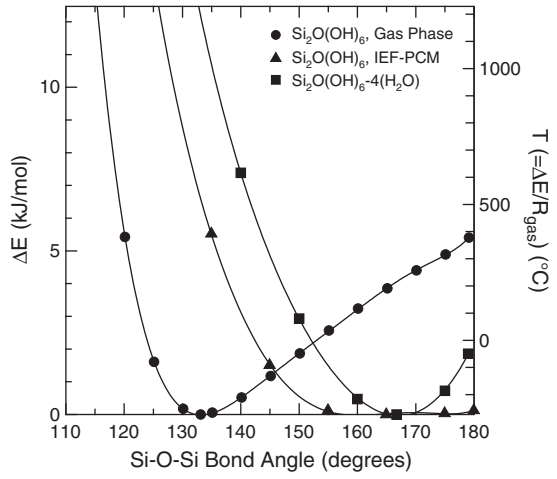

Fig. 8. Potential energy surface for the gas phase dimer, implicitly solvated dimer (IEF-PCM), and explicitly solvated dimer (4 additional water molecules) as a function of bridging angle (Si–O–Si). All other molecular coordinates are allowed to relax to a minimum-energy structure. Thermal energy due to temperature is shown on the right axis to show the distribution of dimer bridging angles that will be present at a given temperature.

4.2. Comparison to NMR studies

NMR studies have been carried out on a wide range of alkaline silicate solutions that differ in choice of alkali element, alkali concentration, and silica concentration (Kinrade and Swaddle, 1988a,b; Kinrade and Pole, 1992; Vallazza et al., 1998; Tanaka and Takahashi, 1999; Cho et al., 2006; Haouas and Taulelle, 2006; Knight et al., 2007); however, despite the large parameter space, only one of the solutions in this study has been previously investigated via NMR measurements. Knight et al. (2007) studied a solution containing 1 m SiO_2 and 1 m KOH, corresponding to a K_2O/SiO_2 ratio of 0.5. The Raman spectrum for this solution is shown in Fig. 9a. Knight et al. determined that this solution contained forty-eight geometrically distinct silicate oligomers, forty-one of which account for 85% of the silicon in solution (concentrations were not obtained for the other seven oligomers). Clearly it is impossible to distinguish quantitatively the contributions from each of these oligomers in the Raman spectrum; however, forty-four of the forty-eight species identified

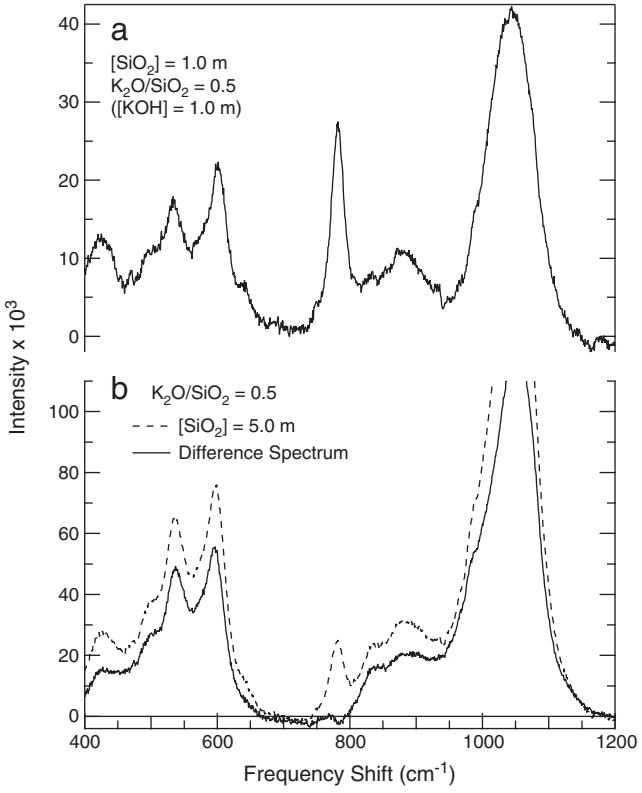

Fig. 9. a.) Raman spectrum of a silicate solution with $[SiO_2] = 1$ molal and $K_2O/SiO_2 = 0.5$, previously studied by NMR (Knight et al., 2007). b.) Raman spectrum of a silicate solution with $[SiO_2] = 5$ molal and $K_2O/SiO_2 = 0.5$ (dashed line), and the difference of spectra with $[SiO_2] = 5$ molal and 1 molal, $K_2O/SiO_2 = 0.5$ (solid line).

by NMR contain three or four membered rings (the only exceptions being the monomer, dimer, linear trimer, and the linear tetramer), which will contribute to the peaks in the 500–600 cm^{-1} range (Galeener et al., 1984).

According to Knight et al. (2007), the monomer concentration in a solution with total [Si] = 1 m and $K_2O/SiO_2 = 0.5$ is 54 millimolal, or 5.4% of the total silica in solution. Fig. 9a clearly shows, therefore, that the monomer symmetric stretch has a much higher Raman activity than Si–O–Si bending modes or ring breathing modes. Fig. 9b shows a comparison between the solution studied by Knight et al. and one with five times the total amount of silica. The dashed spectrum is of the solution with total [Si] = 5 m and $K_2O/SiO_2 = 0.5$ (also shown in Fig. 5c), and the solid line is a difference spectrum between the dashed spectrum and the spectrum in Fig. 9a. All of the peaks in the difference spectrum are reduced in intensity, but the monomer peak vanishes entirely (within background subtraction error), indicating that the monomer peak intensity is essentially constant between 1 and 5 molal total SiO_2 at $K_2O/SiO_2 = 0.5$.

4.3. Concentration dependence of Raman intensity

Fig. 10 shows relative band intensities in the experimental Raman spectra, as measured by peak area. The intensity (area) of the monomer peak (735–800 cm^{-1}, Fig. 10a) changes nonlinearly with concentration. At $K_2O/SiO_2 = 0.8$, the monomer peak intensity rises with Si concentration, but the magnitude of the rise decreases slightly with [Si]. As K_2O/SiO_2 declines, this decrease becomes more pronounced, so that at $K_2O/SiO_2 = 0.5$, the monomer peak intensity remains essentially constant with rising [Si] above ~1 molal. In contrast, the intensities of the characteristic deprotonated-species peaks (850–1125 cm^{-1}, Fig. 10b) and oligomer peaks (475–650 cm^{-1}, Fig. 10c) scale roughly linearly with total SiO_2 concentration, though a minor dependence on K_2O/SiO_2 ratio remains. The nearly linear variation of the oligomer and deprotonated-species peak areas with concentration suggests that their relative peak areas are proportional to species' concentrations.

Assuming this proportionality holds true for the monomer species as well, we interpret the observed non-linear variation with concentration (Fig. 10a) as confirmation that as more SiO_2 is added to the solution, the proportion of dissolved SiO2 in oligomeric structures is increased. Even at 5–100 millimolal Si ($K_2O/SiO_2 = 0.8$), the monomer peak area does not scale linearly with concentration, implying that polymerization occurs in dilute solutions as well. In more concentrated solutions (1–5 molal), when $K_2O/SiO_2 = 0.5$, the area of the monomer peak is essentially constant over a five-fold increase in total Si concentration (Fig. 10a). A similar effect was inferred by Newton and Manning (2008) near the second critical end point in the system SiO_2–H_2O based on experimental measurements of quartz solubility and a thermodynamic mixing model for solute silica.

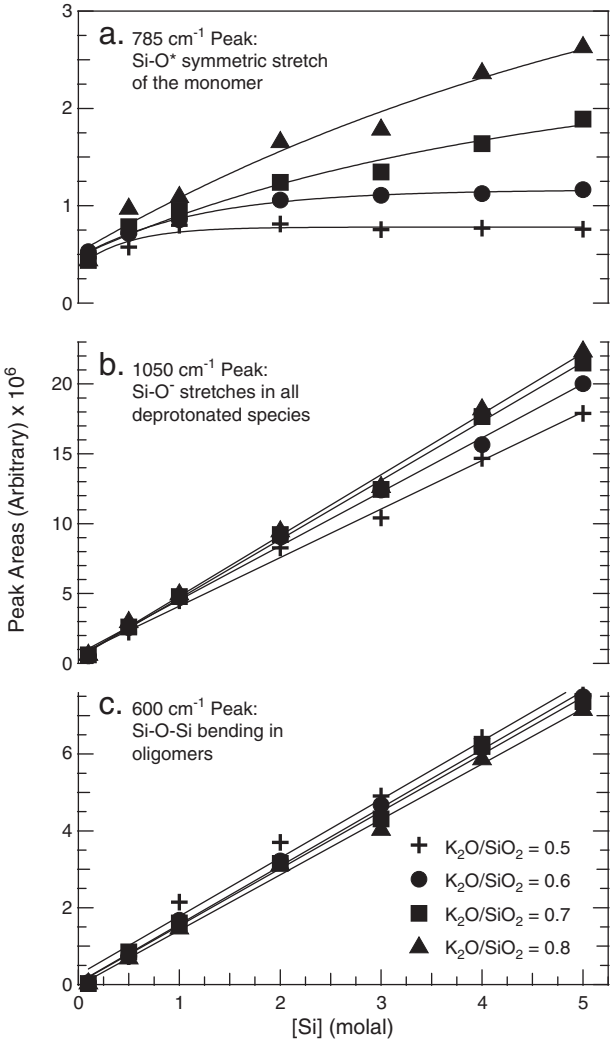

Fig. 10. Measured intensity (area) of a.) the monomer peak (735–800 cm^{-1}), b.) the oligomer peak (475–650 cm^{-1}), and c.) the deprotonation peaks (850–1125 cm^{-1}). While the increases in the oligomer peak and the deprotonation peak appear to scale roughly linearly with concentration, with a slight dependence on the K_2O/SiO_2 ratio, the monomer peak area is non-linear and depends greatly on the K_2O/SiO_2 ratio.

4.4. Concentration and pH dependence of silica speciation

To determine the degree of silica polymerization in a solution relative to that at other compositions and/or conditions, we took the ratio of the oligomer peak area (A_o; 475–650 cm^{-1}) to the monomer peak area (A_m; 735–800 cm^{-1}) of each experimental spectrum. The different Raman cross-sectional areas mean that this peak area ratio is proportional, but not equal, to concentration ratios of oligomeric species to monomers. Mysen (2010) proposed that the Si–OH stretching modes at 875 cm^{-1} may have the same Raman cross-sectional area as Q^0 species, but as noted above, our data suggest that it is not possible to distinguish quantitatively the discrete contributions from Q^0, Q^1, Q^2, and possibly other species in this region. We therefore use the easily resolvable Si–O–Si symmetric mode for our peak area ratios.

The experimental Raman spectra show that silica polymerization depends on both the total concentration of silica in solution and

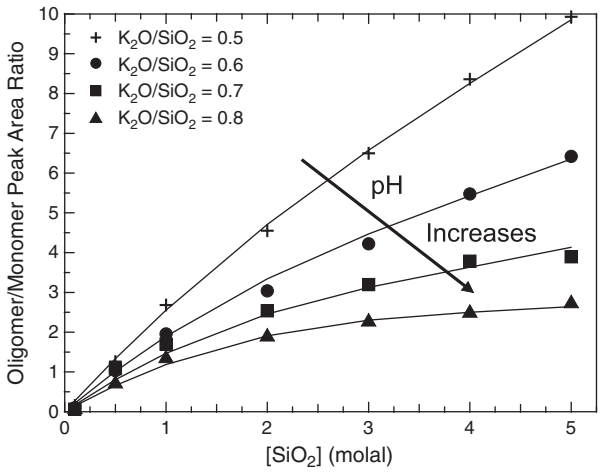

Fig. 11. Ratio of the measured intensity (area) of the oligomer peak (475–650 cm^{-1}) to the monomer peak (735–800 cm^{-1}) as a function of SiO_2 concentration and K_2O/SiO_2 ratio. Regression of the data to Eq. ((1)) is shown by the solid lines.

the K_2O/SiO_2 ratio. This can be seen in Fig. 11, in which variation in calculated peak area ratios (A_o/A_m) with SiO_2 and K_2O concentrations (in molal) are fitted to:

$$\frac{A_o}{A_m} = \left[0.08\left(\frac{K_2O}{SiO_2}\right)^{2.44}\right][K_2O]^3 + \left[-0.43\left(\frac{K_2O}{SiO_2}\right)^{-0.27}\right][K_2O]^2 + \left[1.05\left(\frac{K_2O}{SiO_2}\right)^{-2.29}\right][K_2O] \quad (1)$$

($R^2 = 0.9960$). Increasing Si concentration yields increasing A_o/A_m at all K_2O/SiO_2. As illustrated in Fig. 11, the higher the K_2O/SiO_2 ratio at a given SiO_2 concentration, the more depolymerized the system becomes. Increasing SiO_2 concentration is more effective at polymerization in systems with low K_2O/SiO_2 ratios than it is in systems with high K_2O/SiO_2 ratios. Notably, however, oligomers were detected in solutions as dilute as 50 millimolal silica, as evidenced by the presence of a small peak at ~600 cm^{-1} (Fig. 5a). This is consistent with the observation, by fast atom bombardment mass spectrometry, of trimers and tetramers in dilute (1–85 millimolal) silicate solutions (Tanaka and Takahashi, 1999).

4.5. Elevated pressure and temperature

Fig. 12 shows the relative measure of silica polymerization as a function of *P*, showing that increasing *P* at a constant SiO_2 concentration depolymerizes silica. This is in qualitative agreement with thermodynamic predictions and high-*PT* solubility measurements (Gerya et al., 2005; Newton and Manning 2002, 2003, 2008). Fig. 13 shows the relative measure of silica polymerization as a function of *T*. The spectra show that increasing *T* will also depolymerize the silicate. Assuming near-isochoric behavior, the thermal pressure at 50–200 °C could explain a significant fraction of the observed depolymerization, but it does not appear to account for all of it. This is in qualitative agreement with NMR studies at comparable temperatures (Kinrade and Swaddle, 1988a), though it disagrees with models and high-*PT* solubility measurements (Newton and Manning 2002, 2003, 2008). This disagreement may be due to many factors – e.g., absolute *T* difference, the presence (and concentration) of potassium – and it underscores the need for a systematic Raman investigation of silica polymerization at high *P* and *T* in the hydrothermal diamond anvil cell.

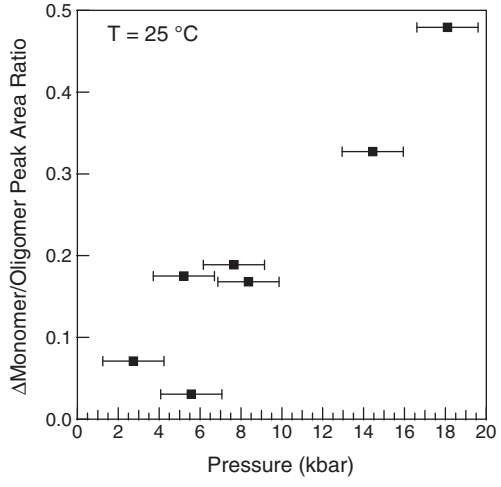

Fig. 12. Difference between the ratio of the measured intensity (area) of the monomer peak (735–800 cm^{-1}) to the oligomer peak (475–650 cm^{-1}) at P and that at 1 bar, at room T. Pressure determined by ruby fluorescence (Mao et al., 1978).

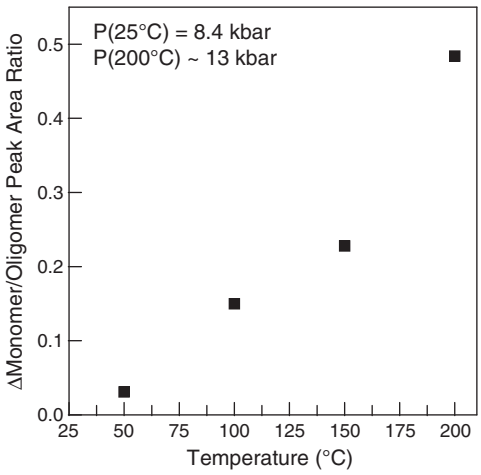

Fig. 13. Difference between the ratio of the measured intensity (area) of the monomer peak (735–800 cm^{-1}) to the oligomer peak (475–650 cm^{-1}) at T and that at 25 °C, as a function of T. Pressure, determined by ruby fluorescence, was 8.4 kbar at 25 °C and increased to ~13 kbar at 200 °C, assuming isochoric behavior.

5. Conclusions

The new results characterize the dependence of polymerization of aqueous silica on total SiO_2 concentration, K_2O/SiO_2 ratio, pressure up to 20 kbar, and temperature up to 200 °C. Increasing the SiO_2 concentration will polymerize the system, but increasing *P*, *T*, or the K_2O/SiO_2 ratio will depolymerize the system. The results also show that the intensities of Raman peaks associated with oligomers and deprotonated species scale linearly with concentration. Assuming that the Raman activity of the monomer is also proportional to its concentration, we have shown that the non-linearity of the monomer peak area with concentration is similar to the behavior observed by Newton and Manning (2008) near the upper critical end point in the H_2O–SiO_2 system. We have also shown that while the $Si_2O(OH)_6$ dimers do exhibit a significant range of Si–O–Si bridging angles, this range is not sufficient to explain the full width of the oligomer peak observed by Zotov and Keppler (2000, 2002). It is therefore highly likely that higher-order oligomers contribute to the broad peak observed at 600 cm^{-1}. These results will establish the foundation of a comprehensive set of hydrothermal diamond anvil cell experiments aimed at measuring polymerization and speciation of silica-rich fluids as a function of temperature, pressure, and concentration.

References

Alexander, G.B., 1954. The polymerization of monosilicic acid. J. Am. Chem. Soc. 76, 2094–2096.
Alexander, G.B., Heston, W.M., Iler, R.K., 1954. The solubiliy of amorphous silica in water. J. Phys. Chem. 58, 453–455.
Anderson, G.M., Burnham, C.W., 1965. Solubility of quartz in supercritical water. Am. J. Sci. 263, 494–511.
Bassett, W.A., Shen, A.H., Bucknum, M., Chou, I.M., 1993. A new diamond-anvil cell for hydrothermal studies to 2.5 GPa and from 190 °C to 1200 °C. Rev. Sci. Instrum. 64, 2340–2345.
Becke, A.D., 1993. Density-functional thermochemistry. III. The role of exact exchange. J. Chem. Phys. 98, 5648–5652.
Cances, E., Mennucci, B., Tomasi, J., 1997. A new integral equation formalism for the polarizable continuum model: theoretical background and applications to isotropic and anisotropic dielectrics. J. Chem. Phys. 107, 3032–3041.
Cho, H., Felmy, A.R., Craciun, R., Keenum, J.P., Shah, N., Dixon, D.A., 2006. Solution state structure determination of silicate oligomers by Si-29 NMR spectroscopy and molecular modeling. J. Am. Chem. Soc. 128, 2324–2335.
De Almeida, W.B., O'Malley, P.J., 1993. Ab-initio infrared and Raman spectra of the $H_3SiO_4^-$ monomeric anionic species. Vib. Spectrosc. 5, 325–335.
Dutta, P.K., Shieh, D.C., 1985. Raman spectral study of the composition of basic silicate solutions. Appl. Spectrosc. 39, 343–346.
Frisch, M.J., Trucks, G.W., Schlegel, H.B., Scuseria, G.E., Robb, M.A., Cheeseman, J.R., Montgomery Jr., J.A., Vreven, T., Kudin, K.N., Burant, J.C., Millam, J.M., Iyengar, S.S., Tomasi, J., Barone, V., Mennucci, B., Cossi, M., Scalmani, G., Rega, N., Petersson, G.A., Nakatsuji, H., Hada, M., Ehara, M., Toyota, K., Fukuda, R., Hasegawa, J., Ishida, M.,

Nakajima, T., Honda, Y., Kitao, O., Nakai, H., Klene, M., Li, X., Knox, J.E., Hratchian, H.P., Cross, J.B., Bakken, V., Adamo, C., Jaramillo, J., Gomperts, R., Stratmann, R.E., Yazyev, O., Austin, A.J., Cammi, R., Pomelli, C., Ochterski, J.W., Ayala, P.Y., Morokuma, K., Voth, G.A., Salvador, P., Dannenberg, J.J., Zakrzewski, V.G., Dapprich, S., Daniels, A.D., Strain, M.C., Farkas, O., Malick, D.K., Rabuck, A.D., Raghavachari, K., Foresman, J.B., Ortiz, J.V., Cui, Q., Baboul, A.G., Clifford, S., Cioslowski, J., Stefanov, B.B., Liu, G., Liashenko, A., Piskorz, P., Komaromi, I., Martin, R.L., Fox, D.J., Keith, T., Al-Laham, M.A., Peng, C.Y., Nanayakkara, A., Challacombe, M., Gill, P.M.W., Johnson, B., Chen, W., Wong, M.W., Gonzalez, C., Pople, J.A., 2004. Gaussian 03, Revision C.02. Gaussian, Inc, Wallingford CT.

Furukawa, T., Fox, K.E., White, W.B., 1981. Raman spectroscopic investigation of the structure of silicate glasses. III. Raman intensities and structural units in sodium-silicate glasses. J. Chem. Phys. 75, 3226–3237.

Galeener, F.L., Barrio, R.A., Martinez, E., Elliott, R.J., 1984. Vibrational decoupling of rings in amorphous solids. Phys. Rev. Lett. 53, 2429–2432.

Gerya, T.V., Maresch, W.V., Burchard, M., Zakhartchouk, V., Doltsinis, N.L., Fockenberg, T., 2005. Thermodynamic modeling of solubility and speciation of silica in H_2O–SiO_2 fluid up to 1300 degrees C and 20 kbar based on the chain reaction formalism. Eur. J. Mineral. 17, 269–283.

Haouas, M., Taulelle, F., 2006. Revisiting the identification of structural units in aqueous silicate solutions by two-dimensional silicon-29 INADEQUATE. J. Phys. Chem. B 110, 3007–3014.

Harris, R.K., Knight, C.T.G., 1983a. Silicon-29 nuclear magnetic resonance studies of aqueous silicate solutions. 5. First-order patterns in potassium silicate solutions enriched with silicon-29. J. Chem. Soc. Faraday Trans. 2 (79), 1525–1538.

Harris, R.K., Knight, C.T.G., 1983b. Silicon-29 nuclear magnetic resonance studies of aqueous silicate solutions. 6. Second-order patterns in potassium silicate solutions enriched with silicon-29. J. Chem. Soc. Faraday Trans. 2 (79), 1539–1561.

Iler, R.K., 1979. The Chemistry of Silica. Wiley.

Kennedy, G.C., Heard, H.C., Wasserburg, G.J., Newton, R.C., 1962. Upper 3-phase region in the system SiO_2–H_2O. Am. J. Sci. 260, 501–521.

Kinrade, S.D., Pole, D.L., 1992. Effect of alkali-metal cations on the chemistry of aqueous silicate solutions. Inorg. Chem. 31, 4558–4563.

Kinrade, S.D., Swaddle, T.W., 1988a. Silicon-29 NMR-studies of aqueous silicate solutions. 1. Chemical-shifts and equilibria. Inorg. Chem. 27, 4253–4259.

Kinrade, S.D., Swaddle, T.W., 1988b. Silicon-29 NMR-studies of aqueous silicate solutions. 2. Transverse ^{29}Si relaxation and the kinetics and mechanism of silicate polymerization. Inorg. Chem. 27, 4259–4264.

Knight, C.T.G., Balec, R.J., Kinrade, S.D., 2007. The structure of silicate anions in aqueous alkaline solutions. Angew. Chem. Int. Ed. 46, 8148–8152.

Krishnan, R., Binkley, J.S., Seeger, R., Pople, J.A., 1980. Self-consistent molecular-orbital methods. 20. Basis set for correlated wavefunctions. J. Chem. Phys. 72, 650–654.

Lazarev, A.N., 1972. Vibrational Spectra and Structure of Silicates. Consultants Bureau, New York.

Licht, S., 1985. pH measurement in concentrated alkaline solutions. Anal. Chem. 57, 514–519.

Manning, C.E., 1994. The solubility of quartz in H_2O in the lower crust and upper mantle. Geochim. Cosmochim. Acta 58, 4831–4839.

Manning, C.E., 2004. The chemistry of subduction-zone fluids. Earth Planet. Sci. Lett. 223, 1–16.

Manning, C.E., 2007. Solubility of corundum + kyanite in H_2O at 700 °C and 10 kbar: evidence for Al–Si complexing at high pressure and temperature. Geofluids 7, 258–269.

Manning, C.E., Wilke, M., Schmidt, C., Cauzid, J., 2008. Rutile solubility in albite-H_2O and $Na_2Si_3O_7$–H_2O at high temperatures and pressures by in-situ synchrotron radiation micro-XRF. Earth Planet. Sci. Lett. 272, 730–737.

Manning, C.E., Antignano, A., Lin, H.A., 2010. Premelting polymerization of crustal and mantle fluids, as indicated by solubility of albite + paragonite + quartz in H_2O at 1 GPa and 350–620 °C. Earth Planet. Sci. Lett. 292, 325–336.

Mao, H.K., Bell, P.M., Shaner, J.W., Steinberg, D.J., 1978. Specific volume measurements of Cu, Mo, Pd, and Ag and calibration of ruby R1 fluorescence pressure gauge from 0.06 to 1 Mbar. J. Appl. Phys. 49, 3276–3283.

Mennucci, B., Tomasi, J., 1997. Continuum solvation models: a new approach to the problem of solute's charge distribution and cavity boundaries. J. Chem. Phys. 106, 5151–5158.

Mennucci, B., Cances, E., Tomasi, J., 1997. Evaluation of solvent effects in isotropic and anisotropic dielectrics and in ionic solutions with a unified integral equation method: theoretical bases, computational implementation, and numerical applications. J. Phys. Chem. B 101, 10506–10517.

Mibe, K., Chou, I.M., Bassett, W.A., 2008. In situ Raman spectroscopic investigation of the structure of subduction-zone fluids. J. Geophys. Res.-Sol. Ea. 113, 8.

Mysen, B.O., 1998. Interaction between aqueous fluid and silicate melt in the pressure and temperatures regime of the Earth's crust and upper mantle. Neues Jahrb. Mineral. Abh. 172, 227–244.

Mysen, B., 2010. Structure of H_2O-saturated peralkaline aluminosilicate melt and coexisting aluminosilicate-saturated aqueous fluid determined in-situ to 800 °C and ~800 MPa. Geochim. Cosmochim. Acta 74, 4123-4139.

Newton, R.C., Manning, C.E., 2002. Solubility of enstatite plus forsterite in H_2O at deep crust/upper mantle conditions: 4 to 15 kbar and 700 to 900 degrees C. Geochim. Cosmochim. Acta 66, 4165–4176.

Newton, R.C., Manning, C.E., 2003. Activity coefficient and polymerization of aqueous silica at 800 °C, 12 kbar, from solubility measurements on SiO_2-buffering mineral assemblages. Contrib. Mineral. Petrol. 146, 135–143.

Newton, R.C., Manning, C.E., 2008. Thermodynamics of SiO_2–H_2O fluid near the upper critical end point from quartz solubility measurements at 10 kbar. Earth Planet. Sci. Lett. 274, 241–249.

Provis, J.L., Duxson, P., Lukey, G.C., Separovic, F., Kriven, W.M., van Deventer, J.S.J., 2005. Modeling speciation in highly concentrated alkaline silicate solutions. Ind. Eng. Chem. Res. 44, 8899–8908.

Ray, N.H., Plaisted, R.J., 1983. The constitution of aqueous silicate solutions. J. Chem. Soc. Dalton Trans. 475–481.

Schmidt, C., Ziemann, M.A., 2000. In-situ Raman spectroscopy of quartz: a pressure sensor for hydrothermal diamond-anvil cell experiments at elevated temperatures. Am. Mineral. 85, 1725–1734.

Scott, A.P., Radom, L., 1996. Harmonic vibrational frequencies: an evaluation of Hartree-Fock, Moller-Plesset, quadratic configuration interaction, density functional theory, and semiempirical scale factors. J. Phys. Chem. 100, 16502–16513.

Sefcik, J., Goddard, W.A., 2001. Thermochemistry of silicic acid deprotonation: comparison of gas-phase and solvated DFT calculations to experiment. Geochim. Cosmochim. Acta 65, 4435–4443.

Sjoberg, S., Hagglund, Y., Nordin, A., Ingri, N., 1983. Equilibrium and structural studies of silicon(IV) and aluminum(III) in aqueous solution. V. Acidity constants of silicic acid and the ionic product of water in the medium range 0.05–2.0 M Na(Cl) at 25 °C. Mar. Chem. 13, 35–44.

Tanaka, H., Takahashi, K., 1999. The identification of chemical species of silica in sodium hydroxide, potassium hydroxide and sodium chloride solutions by FAB-MS. Anal. Sci. 15, 1241–1250.

Tomasi, J., Mennucci, B., Cances, E., 1999. The IEF version of the PCM solvation method: an overview of a new method addressed to study molecular solutes at the QM ab initio level. J. Mol. Struct. Theochem 464, 211–226.

Tossell, J.A., 2005. Theoretical study on the dimerization of $Si(OH)_4$ in aqueous solution and its dependence on temperature and dielectric constant. Geochim. Cosmochim. Acta 69, 283–291.

Tossell, J.A., Sahai, N., 2000. Calculating the acidity of silanols and related oxyacids in aqueous solution. Geochim. Cosmochim. Acta 64, 4097–4113.

Vallazza, E., Bain, A.D., Swaddle, T.W., 1998. Dynamics of silicate exchange in highly alkaline potassium silicate solutions. Can. J. Chem. 76, 183–193.

Zhang, Y.G., Frantz, J.D., 2000. Enstatite–forsterite–water equilibria at elevated temperatures and pressures. Am. Mineral. 85, 918–925.

Zotov, N., Keppler, H., 2000. In-situ Raman spectra of dissolved silica species in aqueous fluids to 900 degrees C and 14 kbar. Am. Mineral. 85, 600–603.

Zotov, N., Keppler, H., 2002. Silica speciation in aqueous fluids at high pressures and high temperatures. Chem. Geol. 184, 71–82.

Zotov, N., Marinov, M., Konstantinov, L., 1996. Degree of structural disorder in sodium metasilicate glass: model for Raman spectra. J. Non-Cryst. Solids 197, 179–191.